crystals

MDPI

Article

Calcium Carbonate Polymorphs Growing in the Presence of Sericin: A New Composite Mimicking the Hierarchic Structure of Nacre

Linda Pastero [1,2,*] and Dino Aquilano [1]

[1] Department of Earth Sciences, University of Turin, Via Valperga Caluso 35, 10125 Torino, Italy; dino.aquilano@unito.it

[2] NIS—Nanostructured Interfaces and Surfaces, University of Turin, Via Quarello 15/A, 10135 Torino, Italy

* Correspondence: linda.pastero@unito.it; Tel.: +39-011-670-5155

Received: 28 May 2018; Accepted: 23 June 2018; Published: 26 June 2018

Abstract: Bioinspired self-assembled composite materials are appealing both for their industrial applications and importance in natural sciences, and represent a stimulating topic in the area of materials science, biology, and medicine. The function of the organic matrix has been studied from the biological, chemical, crystallographic, and engineering point of view. Little attention has been paid to the effect of one of the two main components of the organic matrix, the sericin fraction, on the growth morphology of calcium carbonate polymorphs. In the present work, we address this issue experimentally, emphasizing the morphological effects of sericin on calcite and aragonite crystals, and on the formation of a sericin-aragonite-calcite self-assembled composite with a hierarchic structure comparable to that of natural nacre.

Keywords: biomineralization; calcite; aragonite; sericin; nacre; CO_2; composite; hierarchic structure

1. Introduction

While the structural aspects of biomineralization have been widely studied through many crystallographic techniques, the mechanisms regulating the polymorphs selection or the crystal habit modification in biomineralization need further work, mainly for their crucial importance in the field of the functionalized inorganic-organic composite materials.

A critical challenge in biomineralization is the calcite/aragonite selection in mollusk and gastropod shells; in mollusks, the precipitation of these two $CaCO_3$ polymorphs is modulated in the same shell, the polymorph selection being functional to the structural properties of the mineralized layer. Among the strategies carried out to obtain the synthetic equivalents of nacre [1–4], it is worth remembering a recent one [5], where a synthetic composite very close to both hierarchy and chemical composition of natural nacre was obtained by a classical predesigned matrix directed mineralization method, realizing a chitosan matrix through a freezing-induced process [6,7]. Chitosan is converted to β-chitin by acetylation, and then the matrix is mineralized by flowing $Ca(HCO_3)_2$ in the presence of polyacrylic acid and magnesium. Finally, nacre is obtained by silk fibroin infiltration and hot-pressing of the mineralized matrix.

It is well known that the protein-polysaccharide organic matrix plays a crucial role in the mechanical properties of the mineralized material. Nacre is a robust natural composite made up of of tabular calcium carbonate crystals (95%) which are intimately associated with layers of an organic matrix (5%) that is mainly built of: (i) water-soluble aspartic acid-rich proteins, (ii) glycoproteins, (iii) insoluble highly ordered β-chitin fibers and (iv) Gly-Ala-rich protein hydrogels structurally comparable with silk-fibroin [6,8–17]. The brick-and-mortar structure of nacre reduces crack spreading

inside the structure and confers to the nacre a toughness of increased magnitude in comparison with the sole aragonite [18,19]. Moreover, the large prismatic calcite crystals in the outermost layers of the shell structure are functional to both wear and impact resistance.

Many papers deal with the effect of the shell proteins on calcium carbonate polymorphs stabilization. For example, it is known that chitin fibers act as a template for crystallization of calcite crystals oriented with c-axis perpendicular to the surface of the shell [13].

Each component of the organic matrix in biomineralization has a role in controlling the nucleation of the calcium carbonate polymorphs, their orientation, and morphology, either in the classical way or by means of precursors such as an amorphous carbonate phase (ACC) both in-vivo and in-vitro [15,20–22]. Macromolecules are unanimously considered to be responsible for the selection of the polymorph. As an example, sericin hydrogel contains acidic proteins controlling the morphology and the polymorph. Furthermore, sericin gel in nacre has been suggested as a promoter for aragonite nucleation instead of calcite [15,20,23], through the ability of the acidic functional groups of sericin in binding Ca^{2+} [24].

Proteins associated with calcium mineralization have common features: (i) richness in Ca-coordinating residues, (ii) presence of repetitive sequences, and (iii) common β-sheet secondary structure [8,25]. Some Authors proposed that the regular array of carboxylic groups in the β-sheet structure may promote the epitaxial growth of calcium carbonate in pearls and oyster shells [6,8].

Electron diffraction analysis of the protein/aragonite assembly was carried out by Weiner and coworkers [16,26]. Accordingly, Mann [8] proposed that, at the organic/inorganic interfaces, the cooperation of the electrostatic accumulation of ionic charge at the organic matrix surface by primary cation-binding, the stereochemical requirements and the structural correspondence, favor the nucleation of a biomineral phase. Further, Mann considered the " ... one-to-one geometrical matching between the functional groups of the matrix and the crystallographic lattice dimensions of a specific crystal face in the overlying mineral phase" as an epitaxy between the matrix surface and the crystallizing mineral. The idea of an aragonite matrix enriched in aspartic acid (Asp) residues, initially proposed by Weiner [27], was re-tabled by Mann as well. This polyanionic matrix should be sufficient to control nucleation, polymorphism, and morphology of crystals, while the protein sheet controls the orientation of the calcite primer. Adding soluble shell proteins, does promote the stabilization of aragonite (instead of calcite), while polyacidic proteins drive nucleation and growth of different polymorphs and morphologies. Following these considerations, Mann proposed that the local sequence of charged Asp-residues "could act as a structurally organized nucleation site by binding Ca ions in a configuration corresponding to the 001 plane of aragonite". This epitaxial hypothesis reads: when comparing the Ca-Ca distance in the 001 plane with the periodicity of the organic matrix, an acceptable matching along the [100] axes (4.96 and 4.7 Å respectively) is found. In contrast, a greater mismatch is observed along the [010] axes (7.97 and 6.9 Å respectively), but, along this direction, a good coincidence occurs over a sequence of seven Ca atoms (≅48 Å). It follows that the aminoacid sequence of Asp residues belonging to the matrix substrate, represents optimum binding sites for calcium, thus providing specific nucleation sites.

Recently, Chevalier et al. [25] demonstrated that the formation of the β-sheet structure does not fulfill the conditions required to precipitate ordered arrays of $CaCO_3$ polymorphs, and proved that no specific interaction between the organic and inorganic phases could be evidenced.

In summary, the macromolecules of the organic fraction control polymorphism, orientation, and morphology of carbonate phases in biominerals. Hydrogels interact with the precipitation of carbonate crystals because of (i) the presence of functional groups which may directly interact with reacting ions, (ii) the effect of nucleation sites, and (iii) the interaction between steps and faces with the functional groups. The protein content is less than 2%, but they determine the structural organization and the properties of the composite [7].

Until now, no focused attention has been paid to every possible reticular interface that can be generated when an organized soft matrix (template) promotes on itself the crystallization of an

adsorbed hard phase (one out of the calcium carbonate polymorphs, in our case). This paper aims at reducing this lack of information, and we will strike a blow in favor of the leading role of the template/adsorbate epitaxy. We will deal with the effects of increasing concentrations of sericin in carbonated aqueous solutions, in order to define: (i) the selection of the $CaCO_3$ polymorphs, (ii) the single crystal morphology of the grown polymorphs, and (iii) the interfacial relationships (if any) in the system aragonite/calcite/sericin. The morphological effect will be interpreted on the grounds of the lattice coincidences between sericin (SFLP, silk fibroin like protein in the tables), and calcium carbonate polymorphs. For the sake of simplicity, the fourth index (hk$\bar{i}$l) used in the rhombohedral system (calcite crystal) will be replaced in the text by a point: $\rightarrow$ (hk.l).

2. Materials and Methods

Silk sericin from Bombix moori was purchased from Sigma-Aldrich (Sigma-Aldrich, St. Louis, MO, USA). Calcium chloride, calcium carbonate, ammonium carbonate were analytical grade reagents from Sigma-Aldrich.

Ultrapure water (18 MΩ) was obtained by using an Elga (Veolia Elga LabWater, High Wycombe, UK) Purelab Flex3 ultrapure water system. A calcium carbonate supersaturated solution was obtained by bubbling CO_2 in a calcite/water suspension (0.5 g/L) at room temperature and pressure. The final concentration of the calcium carbonate solution was 5 mM; pH was slightly acidic (5.4). The starting value of the saturation index (SI) of the solution calculated with respect to calcite was −1.41, and −1.55 with respect to aragonite. After equilibration with the atmosphere, the supersaturation values were 0.21 and 0.06 respectively for calcite and aragonite.

Silk sericin cast gel (CG) was obtained following the procedure suggested by Teramoto and coworkers [28]: a solution 1% *w*/*w* of silk sericin was spread on a PP plate (2 mL/cm^2) and dried at 25 °C overnight. After drying, the gel was covered by a thin layer of calcium carbonate saturated solution. The carbon dioxide was allowed to equilibrate with the atmosphere all night long. Calcium carbonate nucleated on the cast gel surface.

In G experiments, calcium carbonate crystal growth was obtained by the slow diffusion of gases released by the thermal decomposition of ammonium carbonate [29,30]. Multiwell cell culture plates were chosen as reactors to ensure the same conditions for each experiment. Each well was filled with 5 mL $CaCl_2$ solution and a variable concentration of sericin to verify the effect of the impurity on the growth of calcium carbonates. One among the wells was filled with $(NH_4)_2CO_3$ saturated solution as a source of carbon dioxide. The multiwell plate was sealed to ensure the saturation of the inner atmosphere in CO_2. A well was filled with $CaCl_2$ solution and a Riedel-De Haën universal pH indicator solution, to monitor the pH value. A control well filled with a calcium chloride solution without sericin was maintained in every batch to separate the effect of sericin from that of the concentration of calcium and carbonate.

The concentration of calcium chloride ranged between 0.1 M and 0.001 M. The concentration of sericin ranged from 1% *w*/*w* to 0.001%.

B experiments were performed by adding sericin to the solution in a concentration ranging from 0.001% to 0.5%. CO_2 was allowed to equilibrate with the atmospheric pressure for two days. Calcium carbonate precipitated as a consequence.

All G, B, and cast gel experiments were performed at room temperature and pressure.

Saturation indexes SI expressed as the ratio of ionic activity product (IAP) to solubility product K_{sp} were calculated for the growth experiments from pure solution by using PHREEQC software (version 3.3.9) [31]. For B and cast gel experiments, the SI of the pure $CaCO_3$ solution equilibrated with the atmosphere was 0.21 with respect to calcite and 0.06 with respect to aragonite, experimentally confirmed by the precipitation of calcite and a few aragonite aggregates whose persistence in the system depends on the rate of the gas equilibration with the atmosphere. Furthermore, in G experiments at saturation with respect to ammonium carbonate in water, the calculations gave very high SI for both calcite and aragonite. SI ranged from 3.6 to 5.6 for calcite

and from 3.4 to 5.4 for aragonite. Such high SI values result in both polymorphs being stable, even in the absence of specific impurities, as experimentally demonstrated. The results of the calculation are reported in Table 1 and in Figure S1.

Table 1. Saturation indexes (SI) and ionic strength (I) of the pure solutions used for B, G and cast gel experiments.

Experiment	Solution	SI Aragonite	SI Calcite	I
B and cast gel	$CaCO_3$ 5 mM	0.06	0.21	1.176×10^{-2}
G	$CaCl_2$ 0.1 M	5.42	5.57	30.75
	$CaCl_2$ 0.01 M	4.41	4.56	29.97
	$CaCl_2$ 0.001 M	3.41	3.56	29.89

The evaluation of the supersaturation in G experiments has to be considered only qualitative. In fact, due to the very high ionic strength of the system, the Debye-Hückel model results were inadequate, and the calculation showed a break-down at 30 mol/kg_w < I < 46 mol/kg_w. The model is not useful for calculations about the fugacity of CO_2. For high ionic strength systems, the specific interaction approach to thermodynamic properties of aqueous solutions should be used [32–35], but this approach is not incorporated in PHREEQC. Moreover, the effect of the addition of sericin to the solution on the supersaturation values with respect to carbonates was disregarded because of the lack of thermodynamic data about sericin.

Polarized optical microscopy was carried out using a Zeiss Axiolab Pol microscope (Carl Zeiss AG, Oberkochen, Germany) equipped with a rotary stage and a JVC 3-CCD KY F55B camera with 750 lines of horizontal resolution and a 60 dB signal-to-noise ratio to capture images and videos.

µ-Raman measurements were performed using a high-resolution confocal µ-Raman system HR800 by Horiba Jobin Yvon equipped with two gratings (1800 and 600 grooves/mm), air-cooled CCD detector, and green polarized laser (solid state Nd, 532 nm, 250 mW). Edge filters (532 nm) and interferential filters complete the system.

SEM imaging was obtained using both a JSM IT300LV High Vacuum–Low Vacuum 10/650 Pa, 0.3–30 kV (JEOL USA Inc., Peabody, MA, USA) equipped with secondary electron (SE) and backscattered electron (BSE) detectors (typical experimental conditions: W filament, EHT 20 kV, working distance 5 mm) and a Zeiss SUPRA 40 (Carl Zeiss AG, Oberkochen, Germany) field emission scanning electron microscope (FE-SEM) based on the 3rd generation GEMINI® column (typical imaging conditions WD = 3 mm, aperture size = 30.00 µm, EHT = 5 kV).

AFM measurements were performed using a DME Igloo SPM microscope (DME, Herlev, Denmark) equipped with a DS95-50E scanner (scan volume 50 × 50 × 5 µm). Data were acquired using MikroMasch Ultrasharp NSC16/Si3N4 Cr-Au back-coated cantilevers with typical resonance frequency 190 kHz, force constant 45 N/m, tip radius lower than 35 nm, and full tip cone angle 40°. All measurements were performed in alternated contact mode.

3. Results and Discussion

From our experiments, we can describe many noticeable effects of sericin on the crystal growth morphology and polymorphs stability of calcium carbonate, the magnitude and significance of these effects depending on the concentration of sericin in solution. The polymorph selection and the morphological effect are closely related and can be emphasized by different experimental setups.

3.1. The Effect of Sericin on the Growth Morphology of Calcite and Aragonite

The effect of sericin as a crystal habit modifier has been studied mainly through the G experiments (see Section 2 for details). From G experiments we obtained both calcite and aragonite polymorphs in pure solution and in the presence of sericin. In fact, very high supersaturation values were reached at the interface between the solution and the surrounding atmosphere, due to the increasing exchange rate in correspondence of the interface. The supersaturation of the pure $CaCO_3$ solution obtained was evaluated using the PHREEQc [31] software (Table 1, Figure S1). The addition of sericin as an impurity into the system has a substantial effect on the nucleation frequency (modifying the supersaturation value and the viscosity of the medium), as well as on the morphology of both polymorphs.

At high supersaturation, aragonite polymorph occurs as aggregates of thin lamellae dominated by the {001} form. In the pure calcium carbonate solution, the aggregates show a very complex morphology, originating "rosetta-like" crystals (Figure 1a) composed by small aragonite platelets with morphology ruled by the {001} form and encompassed by the {010} and {110} forms (Figure 1c and inset). The "rosetta-like" morphology was already described in the literature by Gehrke [36], petals being built by the superposition of single aragonite crystals. Its appearance was ascribed to the sole effect of the supersaturation, as we can confirm.

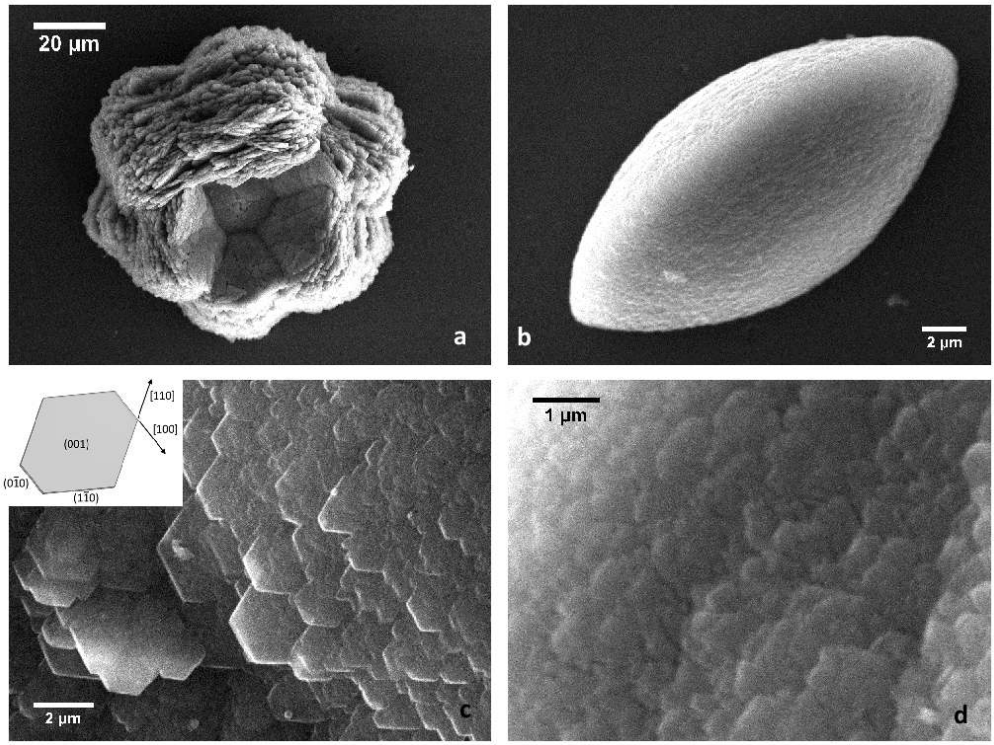

Figure 1. (**a**) "Rosetta-like" aggregate of aragonite grown in pure calcium carbonate solution and (**b**) in the presence of sericin (0.1%), in this case, the aggregate takes on the discoid morphology with smoother surfaces. (**c**) A detail of the aggregate from pure $CaCO_3$ solution, in the inset, the outline of the single crystal of aragonite forming the aggregate, and (**d**) detail of the aggregate grown in the presence of sericin.

In the presence of sericin, the size of the aggregates decreases, aragonite platelets' edges [110] and [100] become unstable and rounded, giving the single crystals an irregular behavior. The whole aspect of the "rosetta-like" aggregates is extremely modified by the presence of the impurity. At high concentrations of sericin, the aggregates take a discoid morphology with smoother surfaces, as shown in Figure 1b. Under quite a different pH and concentration conditions, Cheng and coworkers [24] obtained "rice-like" crystals of calcite, attributing the unusual morphology to the template effect of the

protein on the nucleation and growth of calcite. The simultaneous decrease in aggregates and single platelets size and the loss of stability of the edges of platelets ground the assumption of a synergic effect of sericin on both the supersaturation of the solution and the crystal morphology. The effect of sericin on aragonite morphology becomes evident when its concentration is approximately 0.05% w/w.

Calcite crystals also show a morphological change due to the presence of sericin as an impurity in solution. This originates: (i) in the stabilization of the {00.1}-pinacoid and the {11.0}-prism, and (ii) in the loss of stability of the $[\bar{4}41]$ and $[48\bar{1}]$ edges of the cleavage rhombohedron (Figure 2) which, in turn, produces the appearance of rough {10.4} surfaces. This effect may be recognized since the lower concentration of sericin and rises in magnitude, with the increasing concentration of the impurity.

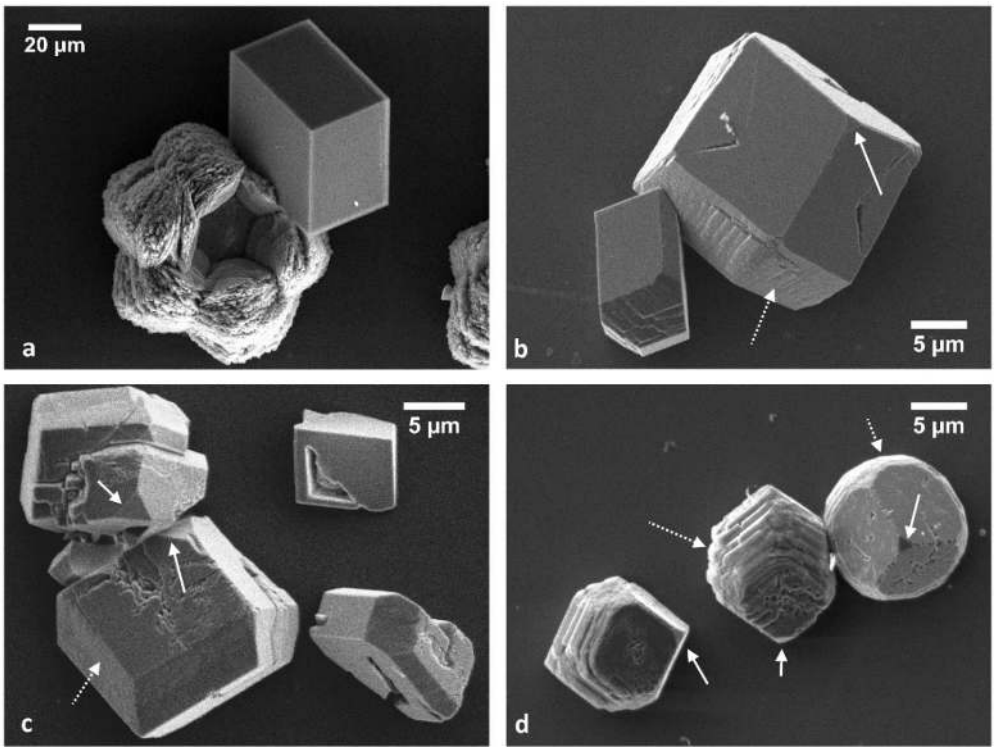

Figure 2. (**a**) calcite crystal and aragonite aggregate grown from pure calcium carbonate solution; (**b**) and (**c**) crystals of calcite grown in the presence of sericin (0.05% w/w), showing the incoming roughness of the cleavage rhombohedron and the appearance of the prism (dotted white arrows) and the pinacoid (solid white arrows). (**d**) The edges of the cleavage rhombohedron $[\bar{4}41]$ and $[48\bar{1}]$ are destabilized by the presence of sericin at higher concentration (0.1% w/w).

The staggering effect of sericin on calcite morphology is particularly significant when considering the growth morphology of prismatic calcite from *Pinna nobilis* shown by Marin in 2004 [37]. Removing the organic matrix from a *Pinna nobilis*' shell by using sodium hypochlorite, the authors obtained calcite crystals with well-developed {00.1} pinacoid and a prism (not indexed because of the lack of reference forms). Our crystals show small pinacoids and more developed prisms; even if the cleavage rhombohedron still dominates the morphology, the trend in morphological modification reflects the biological morphologies.

3.2. The Effect of Sericin on the Polymorph Selection

B and CG experiments are well suited to investigating the mechanism of growth of calcium carbonate spherulites and the role of the impurity in the selection of the polymorph. In general, the spherulitic aggregates take place since the early stages of growth, but only in the presence of

sericin and at the interface between solution and air. In Figure 3a,b, the spherulitic aggregates are characterized by the typical dark extinction cross when observed by polarized optical microscopy.

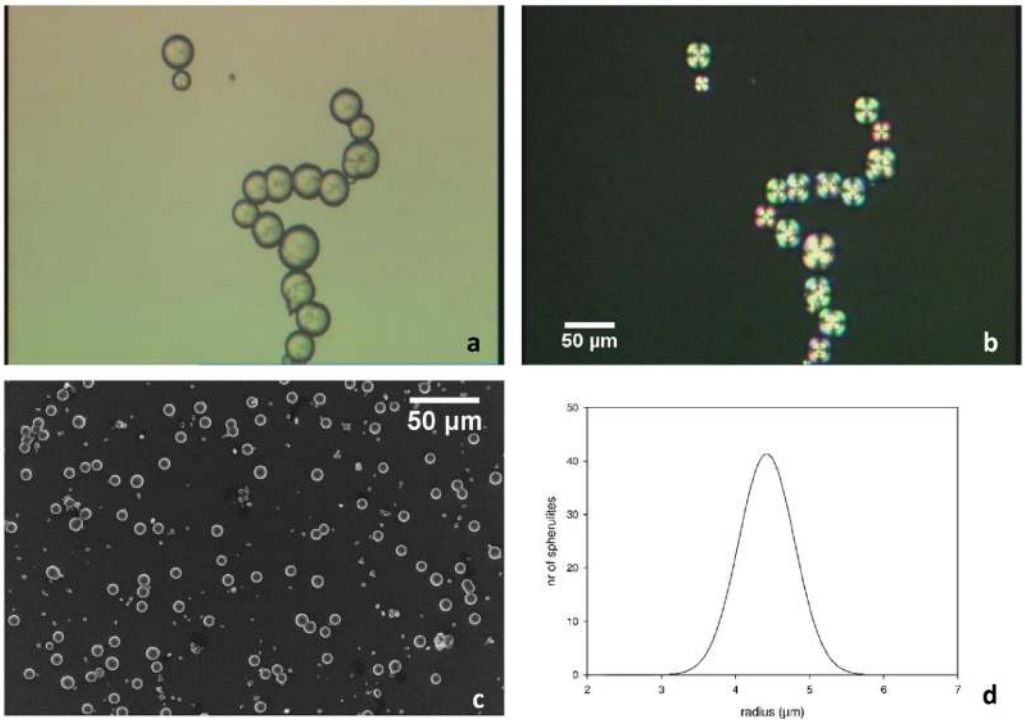

Figure 3. B experiment with 0.5% of sericin: spherulites are the prevailing morphology obtained, their nature of radial aggregates characterized by the typical dark extinction cross in polarized optical microscopy (**a**,**b**). The size distribution of the aggregates is quite uniform (**c**) and represented by a narrow Gaussian curve centered on 4.5 µm (**d**).

Calcium carbonate starts to grow as spherulitic polycrystalline aggregates of aragonite (as will be discussed in the following paragraphs). The size distribution is homogeneously scattered in a very narrow interval: as an example (see Figure 3c), in a B experiment in the presence of 0.5% of sericin, the radius of the aggregates is narrowly distributed around 4.5 µm (Figure 3d). The limited spread in size distribution of the spherulites may be related to two concurring factors: (i) the supersaturation value of the solution, depending on the concentration of calcium carbonate and sericin, and (ii) the nucleation of calcium carbonate on the external surfaces of CO_2 bubbles of selected size, that in turn depends on the pressure inside the vessel.

The presence of bubbles acting as nucleation centers for calcium carbonate is confirmed by the spherical holes at the center of the spherulites. In previous experiments carried out in pure water/carbonate solutions, gas bubbles nucleated heterogeneously onto solid substrates (glass slices, reactor walls) [38,39]. In the present case, bubbles nucleate preferentially at the solution/air interface, owing to the action of the sericin that modifies the ratio between the surface energies between gas and solution. The aggregates grow surrounding the bubbles toward the solution, forming "pearl-necklace" aggregates and single spherulites (Figure 3).

Figure 4a shows a section of two large and connected spherulites: the spherulite on the right is cut near the midpoint and shows the shape and size of the hollow center. The size of the cavity coincides with that of the gas bubble acting as a substrate (4.3 µm), and is close to those obtained by bubbling CO_2 in a calcium carbonate solution at room temperature and pressure by equilibrating the partial pressure of the CO_2 with the atmosphere [38]. Variable concentrations of sericin in solution modify the value of the specific surface energy between gas and solution and, accordingly, the size of the bubbles [39]. Spherulitic structures similar to those here described were already shown by Falini et al.

in 1996 [15], who associated the presence of sericin to the nucleation of the aragonite polymorph. In the paper by Cheng [24], the authors described the formation of "rice-like" and spherical aggregates in the presence of silk fibroin, the spherical ones being morphologically very similar to those obtained in this work, but made up of calcite crystals.

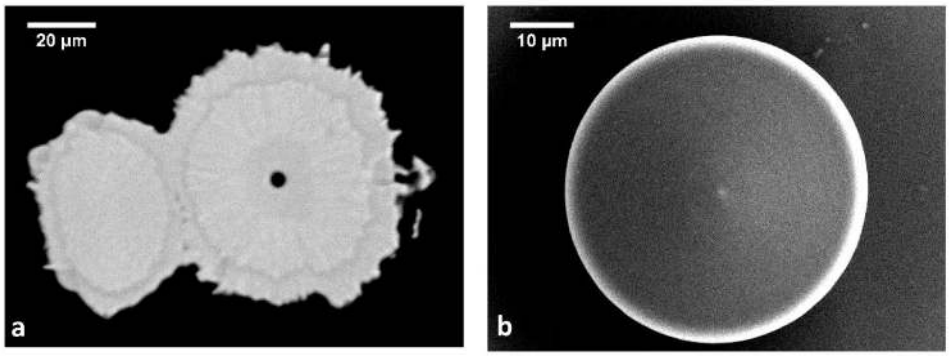

Figure 4. Sections of spherulites: (**a**) the center of the spherulite is a spherical cavity of about 4.3 µm of diameter. At the early stages of evolution, the spherulite grows by concentric layers around the cavity, as shown in (**b**). During the late stages of growth, the outermost layers become irregular (see (**a**)).

The spherulite grows by superposition of concentric shells of calcium carbonate (Figure 4b).

Experimentally, the final size of the spherulites is found to be dependent both on time left for the growth of the aggregates and on the concentration of the impurity. After 12 h of growth, the effect of the concentration of sericin on the size of the spherulites is definitely demonstrated. This means that, even if we did not evaluate the supersaturation of the solution in the presence of such organic impurities, it is reasonable to assume that this value strongly depends on the concentration of the sericin that hinders the nucleation rate, and consequently, increases the size of the spherulites.

At the SEM scale, the surface of the aragonite aggregates seems smooth and somewhat regular, and it is demonstrated to be formed by an aragonite-sericin composite by µ-Raman measurements. At the AFM scale (Figure 5), the aggregates were shown to be covered by nano-sized cobbles with poorly-defined geometries recalling the morphology of aragonite crystals obtained in G experiments (Figure 1d), with the edges rounded by the presence of sericin. Within this first grown layer, aragonite is intimately associated with sericin; in fact, both aragonite and sericin Raman fingerprints are detected.

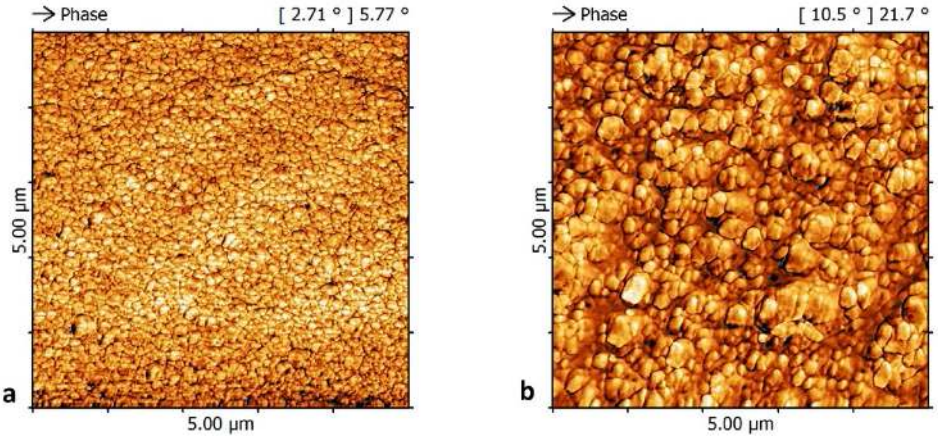

Figure 5. (**a**) AFM-Phase image of the surface of a spherulite grown in a solution containing 0.25% w/w of sericin, (**b**) AFM-Phase image of the surface of a spherulite grown in a solution containing 0.5% w/w of sericin.

The quality of the coverage, the mean size, and the dispersion of the size distribution of the cobbles on the surface of the aragonite aggregate depend on the concentration of the sericin in solution, as proven by the AFM measurements. This dependence is related to the effect of the impurity on the nucleation frequency of the crystals on the spherulites obtained in the most concentrated solution. In fact, in 0.25% w/w grown spherulites (Figure 5a), the cobbles cover the surface of the aggregate uniformly, while in 0.5% w/w grown spherulites (Figure 5b), the coverage is less uniform and the mean size of the cobbles is larger. This observation plays in favor of our early observation about the effect exerted by sericin on the supersaturation of the solution (in G experiments), i.e., at high concentration, sericin lowers the supersaturation even if the concentration of the calcium carbonate in solution is kept constant, thereby decreasing the nucleation rate and increasing the size of the crystals.

As the growth of the composite spherulite proceeds, aragonite aggregates are covered by a rough outer layer of trigonal crystals, as shown in Figure 6a. μ-Raman measurements confirm the presence of both polymorphs as concentric shells around the cavity left by the bubble and the presence of sericin. The signal of sericin is stronger in the inner parts of the aggregate, in correspondence with aragonite, and decreases toward the outer shells made of calcite (Figure 6e and Figure S2). The rough outer part is made by calcite growing with a spindle-like, columnar morphology developing along the radii of the spherulite (Figure 6b,c). This behavior leads to the formation of aggregates, as shown in Figures 6a and 7. However, a weak signal from sericin is detected in the calcite innermost layer of the layered structure. The signal of the sericin is wholly lost only in the very far part of the crystals, where the morphology tends to cure, originating calcite crystals with a complete morphology (Figure 7d).

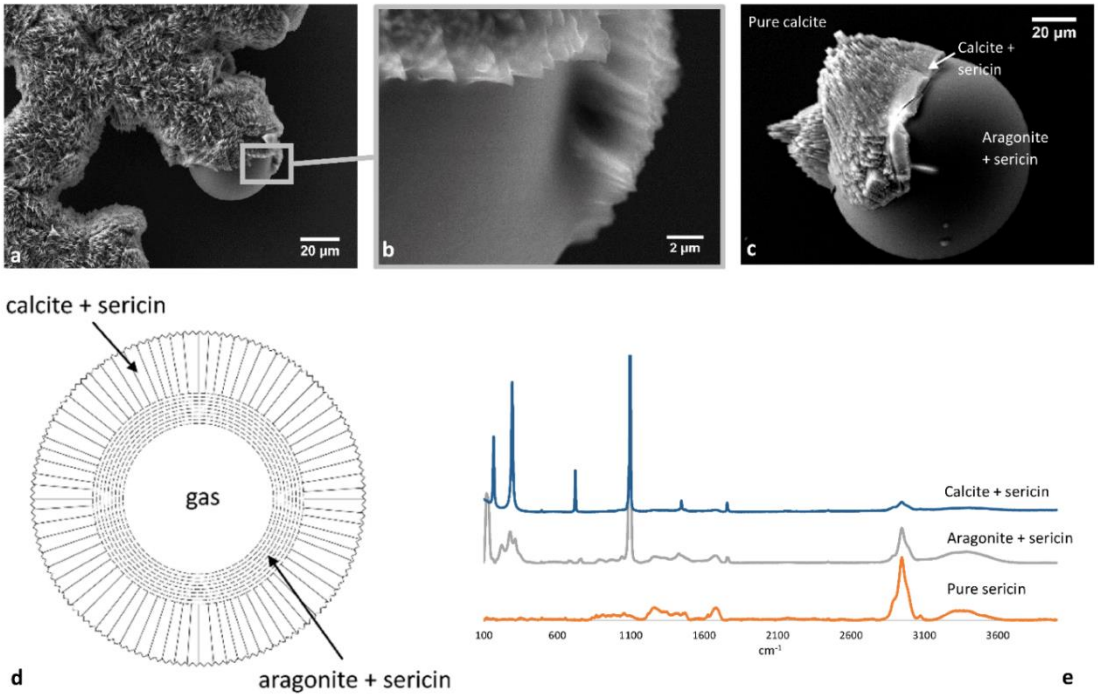

Figure 6. (**a**) a detail of a "pearl-necklace" aggregate of spherulites almost entirely covered by calcite, the trigonal symmetry being stunning evident; (**b**) detail of a spherulitic aggregate from (**a**), not yet wholly covered by columnar calcite crystals; (**c**) a spherulite partially covered by calcite. From μ-Raman measurements, the smoothest part results to be an aragonite-sericin composite, the first layer overgrown is composed by calcite and sericin and the farthest columnar layer by pure calcite (**d**); (**e**) μ-Raman spectra of the layers composing the final spherulite compared with the spectrum of pure sericin.

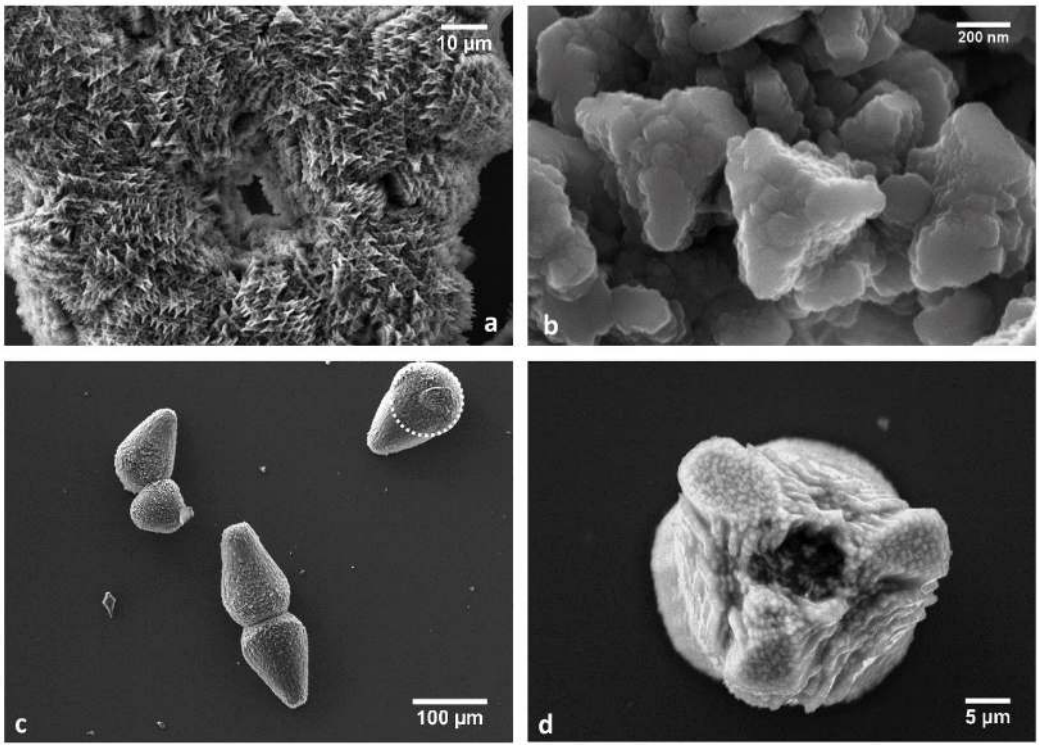

Figure 7. (**a**) Calcite aggregate completely masking the presence of spherulitic aragonite. The image outlines the trigonal symmetry of the crystals; (**b**) a detail of the skeletal calcite crystals growing from the surface of the spherulites; (**c**) when growing without hindrance, calcite gives to the aggregates a "pear-like" morphology. During the early stages of this overgrowth, the presence of the original spherulites is recognizable (dotted circle in the upper right aggregate); (**d**) the rounded shape of the original spherulite is partially masked by the overgrowth of calcite. Calcite skeletal crystals coalesce during growth, forming larger {10.4} surfaces.

The spindle-like columnar crystals are terminated toward the solution by irregular cleavage rhombohedra. In Figure 7a, the orientation of the three-fold axis of calcite toward the observer is clearly evident. At higher magnification, one can recognize skeletal calcite crystals with only the cleavage {10.4} rhombohedron stable surface, encompassed by unstable edges with mean orientation along the $[42\bar{1}]$ and [010] directions. The upper break-off of the crystal is represented by a bumpy {00.1} pinacoid which is macroscopically covered by cobbles, and the elongation of the crystal is due to the presence of an irregular, rounded, and strongly unstable {10.0} prism. This morphology represents the instability of the edges of the cleavage rhombohedron (from G experiments, see Figure 2).

The surface of the aggregate is rough (Figures 6 and 7), and if allowed to grow until the early layers are completely masked by the late ones and not confined, the spherulites take a "pear-like" morphology (Figure 7c), completely covered by calcite crystals with the very unusual morphology already described. The coalescence of many skeletal cleavage rhombohedra yields the formation of larger surfaces, as in Figure 7d. When spherulites are neighboring, during growth they can aggregate, forming the "pearl-necklace" morphologies shown in Figures 3 and 6.

Summing up, it has been shown for the first time what should be the fate of a quasi-stagnant and sericin doped Ca-carbonated aqueous solution that isothermally and spontaneously evolves around CO_2 bubbles from an initial saturation index towards the equilibrium. Ca-carbonate crystallizes at the interface bubble/solution in the form of aragonite during the early stages of growth and in the form of calcite at the end of the growth, the signal from sericin decreasing from the inner part toward the outermost layers, according to the scheme reported in Figure 6d. This behavior reminds one of the

crystallization sequence in mussels' shells, where an aragonite floor sets up in the inner part of the shell, intimately involved with the shell proteins, and followed by a thick layer of columnar calcite.

3.3. Lattice Coincidences between Aragonite (001) and Calcite (00.1) for Epi-Growth on Sericin (001)

As demonstrated in many previous papers, the 2D-epitaxial growth may be considered a common thread for the modification of a crystal growth habit and phase stabilization [40–44]. In the case of sericin and calcium carbonate polymorphs, we started from the considerations by Mann [8] about the matching of the Ca-Ca distances in the 001 plane of aragonite along the directions [010] and [100]. In detail, we remarked at first that: (i) a close matching occurs between the vectors $2 \times [100]_{Ar}$ = 9.922 Å and $2 \times [1/2\ 00]_{SFLP}$ = 9.5 Å, corresponding to a linear misfit of −4.4%, and (ii) a greater mismatch is observed between $[010]_{Ar}$ = 7.9672 Å and $[010]_{SFLP}$ = 6.9 Å, corresponding to a linear misfit of −15.4% that does not fulfill the epitaxy constraints. The linear misfits going in the same sense, the resulting misfit between the areas forming the 2D coincidence cell is dramatic. In fact, the coincidence cell of aragonite (001) has a multiplicity (2×), and the corresponding multiplicity of SFLP (001) is (1×), i.e., the areas of the coincidence cells are 79.05 $Å^2$ for aragonite and 65.55 $Å^2$ for sericin, respectively. Hence, the misfit of the two areas reaches the value of 20.59%, and accordingly, the associated probability of epitaxy is excluded.

According to the suggestion proposed in the Mann's paper, we found a coincidence lattice (Table 2 and 8b in Table 3) fulfilling the linear geometry conditions for epitaxy; however, the area of the corresponding 2D coincidence mesh is so high that it would occupy only the eleventh position in the ranking drawn in Table 3.

In the case of the coupling calcite/sericin, the unit cell of the host sericin substrate is the same as before, while the cell area for the form {001} of calcite is given by the scalar product $[100] \times [010] = 4.9896 \times 4.9896 \times \cos 30^\circ = 21.5606\ Å^2$.

Moreover, we also tested the interface between $(00.1)_{Cc}/(001)_{SFLP}$ (Tables 4 and 5). It is worth outlining that the rotation angle indicates the angle between the vectors [100] of the two mutually rotated cells.

It is interesting to notice that, in the case of sericin on calcite, the surface lattice coincidences are not as good as in the case of sericin on aragonite, mainly due to the high angular misfit that lead to incremental errors in the coincidence areas.

In order to evaluate the hypothetical effect of sericin on the transition between aragonite in the inner part of the aggregate to calcite in the outermost layer, we checked the opportunity of good epitaxial agreement between calcite and aragonite. Given that the most developed form of aragonite in our spherulitic growth is represented by the (001) face, and that, experimentally, we found that calcite grows radially from the surface of the aragonite layer toward the solution with the three-fold axis almost perpendicular to the surface of the spherulite, we also checked the potential coincidences between the $(001)_{Ar}$ and the $(00.1)_{Cc}$ (Tables 6 and 7).

The coincidences between the $(001)_{Ar}$ and the $(00.1)_{Cc}$ are extraordinarily good, providing further proof of the control exerted by the substrate (aragonite) on the orientation of the guest phase (calcite).

Table 2. Comparison between host (sericin) and guest (aragonite) surface cells.

Host Substrate (SFLP) Form {001}	**Guest Crystal (Aragonite) Form {001}**
Unit cell (Å): $[100] \times [010] = 9.5 \times 6.9 = 65.55\ Å^2$	Unit cell cell (Å): $[100] \times [010] = 4.9611 \times 7.9672 = 39.526\ Å^2$

Table 3. 2D-coincidence cells at the interface (001)Ar/(001)SFLP.

2D-Coincidence Cells	Cell Vectors (Å)	Cell Vectors (Å)	Linear Misfit (Δ%)	Notes
(1a)	$-2 \times [1/2\ 00] = 9.5$	$-[110] = 9.3855$	−1.22	Rotation angle 55°
	$1/2[1\bar{6}0] = 21.238$	$[4\bar{1}0] = 21.384$	+0.69	Angular misfit: **2.63°**
Area (Å^2) and 2D-cell multiplicity	**196.65 (3×)**	**197.63 (5×)**	**+0.5**	Opposite linear misfits
(1b)	$2 \times [1/2\ 00] = 9.5$	$[110] = 9.3855$	−1.22	Rotation angle 58.5°
	$-1/2\ [160] = 21.238$	$[3\bar{2}0] = 21.804$	+2.66	Angular misfit: **2.12°**
Area (Å^2) and 2D-cell multiplicity	**196.65 (3×)**	**197.63 (5×)**	**+0.5**	Opposite linear misfits
(2)	$-[120] = 16.754$	$[1\bar{2}0] = 16.689$	−0.39	Rotation angle 52°
	$1/2\ [\bar{3}20] = 15.832$	$-[310] = 16.88$	+6.61	Angular misfit: **2.16°**
Area (Å^2) and 2D-cell multiplicity	**262.2 (4×)**	**276.682 (7×)**	**+5.52**	Opposite linear misfits
(3a)	$-[120] = 16.754$	$-[120] = 16.689$	−0.39	Rotation angle 20°
	$[2\bar{1}0] = 20.214$	$4 \times [100] = 19.844$	−1.86	Angular misfit: **2.71°**
Area (Å^2) and 2D-cell multiplicity	**327.75 (5×)**	**355.734 (9×)**	**−8.53**	Linear misfits in the same sense
(3b)	$[1\bar{2}0] = 16.754$	$[3\bar{1}0] = 16.882$	+0.76	Rotation angle 25°
	$[2\bar{1}0] = 20.214$	$4 \times [100] = 19.844$	+1.95	Angular misfit: **2.26°**
Area (Å^2) and 2D-cell multiplicity	**327.75 (5×)**	**355.734 (9×)**	**−8.53**	Linear misfits in the same sense
(4a)	$-[120] = 16.754$	$-[120] = 16.689$	−0.39	Rotation angle 17°
	$1/2\ [3\bar{6}0] = 25.131$	$2 \times [2\bar{1}0] = 25.45$	+1.27	Angular misfit: **0.56°**
Area (Å^2) and 2D-cell multiplicity	**393.30 (6×)**	**395.26 (10×)**	**+0.5**	Opposite linear misfits
(4b)	$-[120] = 16.754$	$-[120] = 16.689$	−0.39	Rotation angle 17°
	$1/2\ [1.1\bar{0}.0] = 34.825$	$[3\bar{4}0] = 35.1729$	+0.99	Angular misfit: **0.56°**
Area (Å^2) and 2D-cell multiplicity	**393.30 (6×)**	**395.26 (10×)**	**+0.5**	Opposite linear misfits
(4c)	$-[120] = 16.754$	$-[120] = 16.689$	−0.39	Rotation angle 17°
	$1/2[5\bar{2}0] = 24.732$	$5 \times [100] = 24.8055$	+0.297	
Area (Å^2) and 2D-cell multiplicity	**393.30 (6×)**	**395.26 (10×)**	**+0.5**	Opposite linear misfits
(4d)	$[1\bar{2}0] = 16.754$	$[310] = 16.882$	+0.75	Rotation angle **84°**
	$-1/2\ [360] = 25.131$	$2 \times [2\bar{1}0] = 25.45$	+1.27	Angular misfit: **0.25°**
Area (Å^2) and 2D-cell multiplicity	**393.30 (6×)**	**395.26 (10×)**	**+0.5**	Linear misfits in the same sense

Table 3. *Cont.*

2D-Coincidence Cells	Cell Vectors (Å)	Cell Vectors (Å)	Linear Misfit (Δ%)	Notes
(4e)	[1$\bar{2}$0] = 16.754	[310] = 16.882	+0.75	Rotation angle **85°**
	−1/2 [520] = 24.732	[1$\bar{3}$0] = 24.411	−1.31	Angular misfit: **1.90°**
Area (Å^2) and 2D-cell multiplicity	**393.30 (6×)**	**395.26 (10×)**	**+0.5**	Opposite linear misfits
(5)	[1$\bar{2}$0] = 16.754	[3$\bar{1}$0]=16.882	+0.76	Rotation angle 27°
	1/2 [540] = 27.4682	−3 × [110] = 28.1565	+2.50	Angular misfit: **0.63°**
Area (Å^2) and 2D-cell multiplicity	**458.85 (7×)**	**474.312 (12×)**	**+3.37**	Linear misfits in the same sense
(6a)	−1/2[360] = 25.131	−[130] = 24.411	−2.95	Rotation angle 23°
	−[2$\bar{1}$0] = 20.214	− 4 × [100] = 19.844	−1.86	Angular misfit: **2.86°**
Area (Å^2) and 2D-cell multiplicity	**491.625 (7.5×)**	**474.312 (12×)**	**−3.65**	Linear misfits in the same sense
(6b)	1/2 [1$\bar{8}$0] = 28.006	3 × [1$\bar{1}$0] = 28.156	+0.54	Rotation angle 23°
	[2$\bar{1}$0] = 20.214	4 × [100] = 19.844	−1.86	Angular misfit: **2.86°**
Area (Å^2) and 2D-cell multiplicity	**491.625 (7.5×)**	**474.312 (12×)**	**−3.65**	Linear misfits in the same sense
(7)	1/2 [3.$\overline{10}$.0] = 37.327	4 × [1$\bar{1}$0] = 37.542	+0.57	Rotation angle 10°
	−[230] = 28.098	−3 × [110] = 28.1565	+0.21	Angular misfit: **nil**
Area (Å^2) and 2D-cell multiplicity	**950.475 (14.5×)**	**948.624 (24×)**	**−0.19**	Linear misfits in the same sense
(8a)	2 × [1/2 00] = 9.5	2 × [100] =9.922	+4.44	Rotation angle 0°
S. Mann coincidence cell	[010] = 6.9	[010] =7.9672	+15.46	Angular misfit: **0°**
Area (Å^2) and 2D-cell multiplicity	**65.55 (1×)**	**79.052 (2×)**	***+20.6***	Linear misfits in the same sense
(8b)	2 × [1/2 00] = 9.5	2 × [100] = 9.922	+4.44	Rotation angle 0°
S. Mann multiple cell	7 × [010] = 48.3	6 × [010] = 47.83	−1.03	Angular misfit: **0°**
Area (Å^2) and 2D-cell multiplicity	**458.85 (7×)**	**(12×)**	***+3.43***	Opposite linear misfits

Table 4. Comparison between host (sericin) and guest (calcite) surface cells.

Host Substrate (SFLP) Form {001}	Guest Crystal (Calcite) Form {001}
Unit cell: [100] × [010] = 65.55 Å^2	Unit cell: [100] × [010] = 21.5606 Å^2

Table 5. 2D-coincidence cells at the interface (00.1)Cc/(001)SFLP. (1a) and (1b) correspond to the same mutual position of the two lattices: this proves that both area and angular misfit play against the epitaxy.

2D-Coincidence Cells	Cell Vectors (Å)	Cell Vectors (Å)	Linear Misfit (Δ%)	Notes
(1a)	3 × [010] = 20.7	4 × [010] = 19.9584	−3.72	Rotation angle 0°
	[100] = 9.5	[210] = 8.6422	−9.92	Angular misfit: **0°**
Area (Å^2) and 2D-cell multiplicity	**196.65 (6×)**	**172.484 (8×)**	**−14.01**	Linear misfits in the same sense
(1b)	3 × [010] = 20.7	4 × [010] = 19.9584	−3.72	Rotation angle 0°
	1/2 [1$\bar{2}$0] = 8.376	[1$\bar{1}$0] = 8.6422	+3.18	Angular misfit: **4.54°**
Area (Å^2) and 2D-cell multiplicity	**98.325 (3×)**	**86.2426 (4×)**	**−14.01**	Linear misfits in the same sense
	−1/2 [120] = 8.376	[1$\bar{1}$0] = 8.6422	+3.18	Rotation angle 70°
	−[210] = 20.214	−4 × [010] = 19.9584	−1.28	Angular misfit: **5.50°**
Area (Å^2) and 2D-cell multiplicity	**98.325 (3×)**	**86.2426 (4×)**	**−14.01**	Opposite linear misfits
(2a)	1/2 [120] = 8.376	[120] = 8.6422	+3.18	Rotation angle 8°
	[100] = 9.5	[210] = 8.6422	−9.92	Angular misfit: **4.54°**
	65.55 (2×)	**64.682 (3×)**	**−1.34**	Opposite linear misfits
(2b)	1/2 [1$\bar{2}$0] = 8.376	[210] = 8.6422	+3.18	Rotation angle 58°
	[100] = 9.5	[120] = 8.6422	−9.92	Angular misfit: **4.54°**
	65.55 (2×)	**64.682 (3×)**	**−1.34**	Opposite linear misfits
(2c)	[1$\bar{2}$0] = 16.752	3×[100] = 14.9688	**−11.91**	Rotation angle 90°
	1/2 [100] = 4.75	[010] = 4.9896	+5.04	Angular misfit: **4.54°**
	65.55 (2×)	**64.682 (3×)**	**−1.34**	Opposite linear misfits
(2d)	−2 × [010] = 13.8	[2$\bar{1}$0] = 13.2012	−4.53	Rotation angle 43°
	1/2 [100] = 4.75	[110] = 4.9896	+5.04	Angular misfit: **10.89°**
	65.55 (2×)	**64.682 (3×)**	**−1.34**	Opposite linear misfits
(2e)	−2 × [010] = 13.8	[1$\bar{2}$0] = 13.2012	−4.53	Rotation angle 19°
	−1/2 [100] = 4.75	−[110] = 4.9896	+5.04	Angular misfit: **10.89°**
	65.55 (2×)	**64.682 (3×)**	**−1.34**	Opposite linear misfits
(2f)	−1/2 [140] = 14.5946	3 × [100] = 14.9688	+2.564	Rotation angle 82°
	1/2 [100] = 4.75	[010] = 4.9896	+5.04	Angular misfit: **11.006°**
	65.55 (2×)	**64.682 (3×)**	**−1.34**	Linear misfits in the same sense

Table 5. *Cont.*

2D-Coincidence Cells	Cell Vectors (Å)	Cell Vectors (Å)	Linear Misfit (Δ%)	Notes
(3)	$[1\bar{3}0] = 22.776$	$[1\bar{4}0] = 22.865$	+0.39	Rotation angle 35°
	$1/2\,[100] = 4.75$	$[110] = 4.9896$	+5.04	Angular misfit: **5.54°**
	98.325 (3×)	**107.803 (5×)**	**+9.64**	Linear misfits in the same sense
(4)	$1/2\,[300] = 14.25$	$[230] = 13.20$	−7.94	**?**
	$-1/2\,[160] = 21.238$	$[3\bar{2}0] = 21.749$	+2.406	**?**
	294.975 (9×)	**107.803 (13×)**	**−5.24**	Opposite linear misfits
(5a)	$1/2\,[1\bar{6}0] = 21.238$	$[2\bar{3}0] = 21.749$	+2.406	Rotation angle 11°
	$-[210] = 20.214$	$-4 \times [110] = 19.9584$	−1.28	Very low angular misfit
	426.075 (13×)	**431.213 (20×)**	**+1.20**	Opposite linear misfits
(5b)	$1/2\,[3\bar{4}0] = 19.839$	$4 \times [100] = 19.9584$	+0.612	Rotation angle 15°
	$-[130] = 22.776$	$-[150] = 22.865$	+0.39	Very low angular misfit
	426.075 (13×)	**431.213 (20×)**	**+1.20**	Linear misfits in the same sense
(5c)	$-1/2\,[160] = 21.238$	$[2\bar{3}0] = 21.749$	+2.406	Rotation angle 50°
	$[\bar{2}10] = 20.214$	$-4 \times [110] = 19.9584$	−1.28	Very low angular misfit
	426.075 (13×)	**431.213 (20×)**	**+1.20**	Opposite linear misfits

Table 6. Comparison between host (calcite) and guest (aragonite) surface cells.

Host Crystal (Calcite) Form {001}	Guest Crystal (Aragonite) Form {001}	Misfit (Δ%)
$[100] = [010] = 4.9896$ $\gamma = 120°$	$[100] = 4.9611$; $[010] = 7.9672$ $\gamma = 90°$	
$2 \times$ Unit cell: $[100] \times [010] \times \cos 30° = 43.121$	Unit cell: $[100] \times [010] = 4.9611 \times 7.9672 = 39.526$	**−9.096**

Table 7. 2D-coincidence cells at the interface (00.1)Cc/(001)Ar.

2D-Coincidence Cells	Cell Vectors (Å)	Cell Vectors (Å)	Linear Misfit (Δ%)	Notes
	[010] = 4.9896	[100] = 4.9611	−0.574	Rotation angle **90°**
	[210] = 8.6422	−[010] = 7.9672	−8.47	
Area (Å^2) and 2D-cell multiplicity	**43.121 (2×)**	**39.526 (1×)**	**−9.096**	Linear misfits in the same sense
	[1$\bar{1}$0] = 8.6422	[1$\bar{1}$0] = 9.3855	+8.60	Rotation angle **0°**
	−[120] = 8.6422	−[110] = 9.3855	+8.60	
Area (Å^2) and 2D-cell multiplicity	**64.681 (3×)**	**79.052 (2×)**	**+22.2**	Linear misfits in the same sense
	2 × [100] = 9.9792	[1$\bar{1}$0] = 9.3855	−6.325	Rotation angle **30°**
	2 × [110] = 9.9792	2 × [100] = 9.9222	−0.574	
Area (Å^2) and 2D-cell multiplicity	**86.242 (4×)**	**79.052 (2×)**	**−9.096**	Linear misfits in the same sense
	−[230] = 13.2012	−[210] = 12.725	−3.74	**(a)**Rotation angle **11°**
	2 × [1$\bar{1}$0] = 17.2844	[1$\bar{2}$0] = 16.6888	−3.56	
Area (Å^2) and 2D-cell multiplicity	**215.605 (10×)**	**197.63 (5×)**	**−9.096**	Linear misfits in the same sense
	[1$\bar{4}$0] = 22.8652	−3 × [010] = 23.9016	+4.53	**(b)**Rotation angle **11°**
	−[230] = 13.2012	−[210] = 12.725	−3.74	
Area (Å^2) and 2D-cell multiplicity	**237.165 (11×)**	**237.156 (6×)**	**+0.04**	Opposite linear misfits
	[320] = 13.2012	[2$\bar{1}$0] = 12.725	−3.74	Rotation angle **52°**
	5×[010] = 24.948	2×[210] = 25.45	+2.012	
Area (Å^2) and 2D-cell multiplicity	**323.4075 (15×)**	**316.208 (8×)**	**−2.28**	Opposite linear misfits
	−[350] = 21.7492	−[320] = 21.8040	+0.252	Rotation angle **8°**
	3 × [1$\bar{1}$0] = 25.9266	[2$\bar{3}$0] = 25.8792	−0.183	
Area (Å^2) and 2D-cell multiplicity	**517.452 (24×)**	**513.838 (13×)**	**−0.703**	Opposite linear misfits
	[2$\bar{3}$0] = 21.7492	−[320] = 21.8040	+0.252	Rotation angle **66°**
	3 × [210] = 25.9266	[2$\bar{3}$0] = 25.8792	−0.183	
Area (Å^2) and 2D-cell multiplicity	**517.452 (24×)**	**513.838 (13×)**	**−0.703**	Opposite linear misfits
	[3$\bar{2}$0] = 21.7492	−[320] = 21.8040	+0.252	Rotation angle **80°**
	2 × [320] = 26.402	[2$\bar{3}$0] = 25.8792	−2.022	
Area (Å^2) and 2D-cell multiplicity	**517.452 (24×)**	**513.838 (13×)**	**−0.703**	Opposite linear misfits

4. Conclusions

Two main effects due to the presence of sericin as an impurity in solution on the growth of calcium carbonate crystals have been experimentally confirmed: (i) a morphological effect on both calcite and aragonite, and (ii) a polymorph-stabilizer effect.

Concerning the first point, aragonite crystal morphologies have been compared in pure solution and in the presence of sericin. Even if the "rosetta-like" aggregates have already been described in the literature, the morphology of the single lamellae of aragonite building up the aggregates is modified by the presence of sericin. The lamellae are dominated by the flat {001} form, and encompassed by almost inexistent {110} and {100} forms. In the presence of sericin, the edges [110] and [010] of the single lamella lose their stability, becoming rounded and irregular. Moreover, the size of the lamellae decreases with the increase in sericin content, demonstrating the effect of sericin on both the supersaturation of the system and the interface energy between aragonite and the solution.

Concerning the calcite crystals, the {00.1}-pinacoid and the {11.0}-prism, usually unstable, are found. Calcite crystals still show the {10.4}-cleavage rhombohedron, but the stabilization of the new forms approaches the morphology to that of the biological prismatic calcite associated to nacre found in the literature. The morphological effect of sericin on calcite is undoubtedly driven by the kinetics of the growth process. In fact, the role of the impurity becomes more and more significant at low supersaturation values with respect to calcium carbonate when the rate of growth of the crystals is lower, and the competition between the kinetics of adsorption of the impurity and the kinetics of growth are comparable.

The effect of sericin on the growth morphology of both polymorphs can be explained in terms of lattice coincidences between the flat and continuous (001) layers of ordered sericin and the 2D-surface cells of both calcite {00.1} and aragonite {001}. This reticular property obviously only fulfills the necessary condition for the epitaxy to occur; however, it proves that the host/guest relation cannot be confined to the interaction between single molecules, being the result of the adhesion of two ordered entities.

The stabilization of aragonite during the early stages of precipitation, even if under moderate supersaturation conditions (that in pure solution bring to the precipitation of the sole rhombohedral calcite), is probably thanks to the good agreement between the surface lattice of aragonite and sericin.

In the presence of CO_2 equilibrating with the atmosphere, carbon dioxide in excess with respect to the atmosphere in the presence of sericin yields small bubbles inside the solution that act as preferential nucleation centers for calcium carbonate. The first layer of calcium carbonate, made by aragonite crystals intimately associated with sericin, grows on the external surface of the bubble. Then, lowering the supersaturation and decreasing the effect of the impurity that is found to be more concentrated in the inner part of the aggregate, calcite nucleates on the former substrate, oriented with the *c*-axis parallel to that of aragonite and with its {00.1} form epitaxially stabilized by the presence of the {001} form of aragonite. It is likely that the effect of sericin on the morphology of calcite could be considered partially responsible for the orientation and morphology of the calcite layer, because of its incomplete coverage; however, the epitaxial agreement between the two polymorphs is strong enough to rule the crystallization of calcite even at lower supersaturation.

Sericin is detectable in the aggregate by μ-Raman measurements and qualitatively decreases from the first mineralized layers in the core of the aggregate toward the external part of the spherulite. Moreover, the bubble encased in the growing calcium carbonate aggregate, segregates the CO_2, making it unavailable to the growing system and originating a confined slightly acid environment that, in turn, can be associated with the local concentration of sericin.

In this way, a three-phased poly-crystalline architecture made by calcium carbonate (in both aragonite and calcite forms) and sericin, radially distributed onto spherical surfaces, mimics the nacre structure. It is worth outlining that this complex object, ruled by three different epitaxies, spontaneously forms in the presence of a CO_2 bubble dipped into a quasi-stagnant aqueous solution

containing calcium carbonate and sericin. As the free CO_2 is ubiquitous near the living organisms, the association between sericin and CO_2 can partially explain the formation of nacre-like structures.

Supplementary Materials: The following are available online at http://www.mdpi.com/2073-4352/8/7/263/s1, Figure S1: Saturation index (SI) of carbonates in G experiments varying the concentration of calcium chloride; Figure S2: (a) μ-Raman spectrum of the sunflower-like spherulitic aggregate showing the vibrational fingerprint of aragonite; (b) μ-Raman spectrum of calcite from G experiments; from (c) to (e) comparison among the μ-Raman spectra of the pure sericin, the inner and outer part of the spherulite, showing the sericin signal decreasing in intensity from the core toward the outermost part of the spherulite.

Author Contributions: Investigation, Methodology, Validation, Software, L.P.; Conceptualization, Writing-Review & Editing, L.P. and D.A.; Formal Analysis D.A.

Funding: This research received no external funding.

Acknowledgments: The Authors would like to thank Salvatore Guastella for FESEM imaging.

Conflicts of Interest: The authors declare no conflict of interest.

References

1. Finnemore, A.; Cunha, P.; Shean, T.; Vignolini, S.; Guldin, S.; Oyen, M.; Steiner, U. Biomimetic layer-by-layer assembly of artificial nacre. *Nat. Commun.* **2012**, *3*, 966. [CrossRef] [PubMed]
2. Liu, R.; Xu, X.; Cai, Y.; Cai, A.; Pan, H.; Tang, R.; Cho, K. Preparation of Calcite and Aragonite Complex Layer Materials Inspired from Biomineralization. *Cryst. Growth Des.* **2009**, *9*, 3095–3099. [CrossRef]
3. Das, P.; Malho, J.-M.; Rahimi, K.; Schacher, F.H.; Wang, B.; Demco, D.E.; Walther, A. Nacre-mimetics with synthetic nanoclays up to ultrahigh aspect ratios. *Nat. Commun.* **2015**, *6*, 5967. [CrossRef] [PubMed]
4. Zhu, B.; Jasinski, N.; Benitez, A.; Noack, M.; Park, D.; Goldmann, A.S.; Barner-Kowollik, C.; Walther, A. Hierarchical Nacre Mimetics with Synergistic Mechanical Properties by Control of Molecular Interactions in Self-Healing Polymers. *Angew. Chem. Int. Ed.* **2015**, *54*, 8653–8657. [CrossRef] [PubMed]
5. Mao, L.-B.; Gao, H.-L.; Yao, H.-B.; Liu, L.; Cölfen, H.; Liu, G.; Chen, S.-M.; Li, S.-K.; Yan, Y.-X.; Liu, Y.-Y.; et al. Synthetic nacre by predesigned matrix-directed mineralization. *Science* **2016**, *354*, 107–110. [CrossRef] [PubMed]
6. Weiner, S.; Addadi, L. Design strategies in mineralized biological materials. *J. Mater. Chem.* **1997**, *7*, 689–702. [CrossRef]
7. Belcher, A.M.; Wu, X.H.; Christensen, R.J.; Hansma, P.K.; Stucky, G.D.; Morse, D.E. Control of crystal phase switching and orientation by soluble mollusc-shell proteins. *Nature* **1996**, *381*, 56–58. [CrossRef]
8. Mann, S. Molecular recognition in biomineralization. *Nature* **1988**, *332*, 119–124. [CrossRef]
9. Falini, G.; Weiner, S.; Addadi, L. Chitin-Silk Fibroin Interactions: Relevance to Calcium Carbonate Formation in Invertebrates. *Calcif. Tissue Int.* **2003**, *72*, 548–554. [CrossRef] [PubMed]
10. Heinemann, F.; Launspach, M.; Gries, K.; Fritz, M. Gastropod nacre: Structure, properties and growth—Biological, chemical and physical basics. *Biophys. Chem.* **2011**, *153*, 126–153. [CrossRef] [PubMed]
11. Keene, E.C.; Evans, J.S.; Estroff, L.A. Matrix Interactions in Biomineralization: Aragonite Nucleation by an Intrinsically Disordered Nacre Polypeptide, n16N, Associated with a β-Chitin Substrate. *Cryst. Growth Des.* **2010**, *10*, 1383–1389. [CrossRef]
12. Mann, S. *Biomineralization: Principles and Concepts in Bioinorganic Materials Chemistry*; Oxford University Press: Oxford, UK, 2001; ISBN 9780198508823.
13. Al-Sawalmih, A.; Li, C.; Siegel, S.; Fabritius, H.; Yi, S.; Raabe, D.; Fratzl, P.; Paris, O. Microtexture and Chitin/Calcite Orientation Relationship in the Mineralized Exoskeleton of the American Lobster. *Adv. Funct. Mater.* **2008**, *18*, 3307–3314. [CrossRef]
14. Addadi, L.; Joester, D.; Nudelman, F.; Weiner, S. Mollusk Shell Formation: A Source of New Concepts for Understanding Biomineralization Processes. *Chem. Eur. J.* **2006**, *12*, 980–987. [CrossRef] [PubMed]
15. Falini, G.; Albeck, S.; Weiner, S.; Addadi, L. Control of Aragonite or Calcite Polymorphism by Mollusk Shell Macromolecules. *Source Sci. New Ser.* **1996**, *271*, 67–69. [CrossRef]
16. Weiner, S.; Traub, W.; Parker, S.B. Macromolecules in Mollusc Shells and Their Functions in Biomineralization [and Discussion]. *Philos. Trans. R. Soc. B Biol. Sci.* **1984**, *304*, 425–434. [CrossRef]

17. Levi-Kalisman, Y.; Falini, G.; Addadi, L.; Weiner, S. Structure of the Nacreous Organic Matrix of a Bivalve Mollusk Shell Examined in the Hydrated State Using Cryo-TEM. *J. Struct. Biol.* **2001**, *135*, 8–17. [CrossRef] [PubMed]
18. Bouville, F.; Maire, E.; Meille, S.; Van de Moortèle, B.; Stevenson, A.J.; Deville, S. Strong, tough and stiff bioinspired ceramics from brittle constituents. *Nat. Mater.* **2014**, *13*, 508–514. [CrossRef] [PubMed]
19. Niebel, T.P.; Bouville, F.; Kokkinis, D.; Studart, A.R. Role of the polymer phase in the mechanics of nacre-like composites. *J. Mech. Phys. Solids* **2016**, *96*, 133–146. [CrossRef]
20. Gotliv, B.-A.; Addadi, L.; Weiner, S. Mollusk Shell Acidic Proteins: In Search of Individual Functions. *ChemBioChem* **2003**, *4*, 522–529. [CrossRef] [PubMed]
21. Weiss, I.M.; Tuross, N.; Addadi, L.; Weiner, S. Mollusc larval shell formation: Amorphous calcium carbonate is a precursor phase for aragonite. *J. Exp. Zool.* **2002**, *293*, 478–491. [CrossRef] [PubMed]
22. Jin, W.; Jiang, S.; Pan, H.; Tang, R. Amorphous Phase Mediated Crystallization: Fundamentals of Biomineralization. *Crystals* **2018**, *8*, 48. [CrossRef]
23. Thompson, J.B.; Paloczi, G.T.; Kindt, J.H.; Michenfelder, M.; Smith, B.L.; Stucky, G.; Morse, D.E.; Hansma, P.K. Direct observation of the transition from calcite to aragonite growth as induced by abalone shell proteins. *Biophys. J.* **2000**, *79*, 3307–3312. [CrossRef]
24. Cheng, C.; Shao, Z.; Vollrath, F. Silk Fibroin-Regulated Crystallization of Calcium Carbonate. *Adv. Funct. Mater.* **2008**, *18*, 2172–2179. [CrossRef]
25. Chevalier, N.R.; Chevallard, C.; Goldmann, M.; Brezesinski, G.; Guenoun, P. $CaCO_3$ Mineralization under β-Sheet Forming Peptide Monolayers. *Cryst. Growth Des.* **2012**, *12*, 2299–2305. [CrossRef]
26. Weiner, S.; Talmon, Y.; Traub, W. Electron diffraction of mollusc shell organic matrices and their relationship to the mineral phase. *Int. J. Biol. Macromol.* **1983**, *5*, 325–328. [CrossRef]
27. Weiner, S.; Hood, L. Soluble protein of the organic matrix of mollusk shells: A potential template for shell formation. *Science* **1975**, *190*, 987–989. [CrossRef] [PubMed]
28. Ito, A.; Nakamura, S.; Aoki, H.; Akao, M.; Teraoka, K.; Tsutsumi, S.; Onuma, K.; Tateishi, T. Hydrothermal growth of carbonate-containing hydroxyapatite single crystals. *J. Cryst. Growth* **1996**, *163*, 311–317. [CrossRef]
29. Gómez-Morales, J.; Hernández-Hernández, Á.; Sazaki, G.; García-Ruiz, J.M. Nucleation and polymorphism of calcium carbonate by a vapor diffusion sitting drop crystallization technique. *Cryst. Growth Des.* **2010**, *10*, 963–969. [CrossRef]
30. Lakshminarayanan, R.; Kini, R.M.; Valiyaveettil, S. Investigation of the role of ansocalcin in the biomineralization in goose eggshell matrix. *Proc. Natl. Acad. Sci. USA* **2002**, *99*, 5155–5159. [CrossRef] [PubMed]
31. Parkhurst, D.L.; Appelo, C.A.J. Description of input and examples for PHREEQC version 3—A computer program for speciation, batch-reaction, one-dimensional transport, and inverse geochemical calculations: U.S. Geological Survey Techniques and Methods. In *U.S. Geological Survey Techniques and Methods, Book 6*; USGS: Reston, VA, USA, 2013; p. 497.
32. Bradley, D.J.; Pitzer, K.S. Thermodynamics of electrolytes. 12. Dielectric properties of water and Debye-Hückel parameters to 350 degree C and 1 kbar. *J. Phys. Chem.* **1979**, *83*, 1599–1603. [CrossRef]
33. Harvie, C.E.; Weare, J.H. The prediction of mineral solubilities in natural waters: The Na-K-Mg-Ca-Cl-SO_4-H_2O system from zero to high concentration at 25 °C. *Geochim. Cosmochim. Acta* **1980**, *44*, 981–997. [CrossRef]
34. Harvie, C.E.; Møller, N.; Weare, J.H. The prediction of mineral solubilities in natural waters: The Na-K-Mg-Ca-H-Cl-SO_4-OH-HCO_3-CO_3-CO_2-H_2O system to high ionic strengths at 25 °C. *Geochim. Cosmochim. Acta* **1984**, *48*, 723–751. [CrossRef]
35. Plummer, N.; Parkhurst, D.L.; Fleming, G.W.; Dunkle, S.A. *A Computer Program Incorporating Pitzer's Equations for Calculation of Geochemical Reactions in Brines*; Water-Resources Investigations Report 88-4153; U.S. Geological Survey: Reston, VA, USA, 1988.
36. Gehrke, N.; Cölfen, H.; Pinna, N.; Antonietti, M.; Nassif, N. Superstructures of calcium carbonate crystals by oriented attachment. *Cryst. Growth Des.* **2005**, *5*, 1317–1319. [CrossRef]
37. Marin, F.; Luquet, G. Molluscan shell proteins. *Comptes Rendus Palevol.* **2004**, *3*, 469–492. [CrossRef]
38. Aquilano, D.; Costa, E.; Genovese, A.; Roberto Massaro, F.; Pastero, L.; Rubbo, M. Hollow rhombohedral calcite crystals encompassing CO_2 microcavities nucleated in solution. *J. Cryst. Growth* **2003**, *247*, 516–522. [CrossRef]

39. Massaro, F.R.; Aquilano, D. Calcite bubbles. The control exerted on the bubble size by solubility and interfacial tension. *Eur. J. Miner.* **2007**, *19*, 339–344. [CrossRef]
40. Aquilano, D.; Pastero, L.; Bruno, M.; Rubbo, M. {1 0 0} and {1 1 1} forms of the NaCl crystals coexisting in growth from pure aqueous solution. *J. Cryst. Growth* **2009**, *311*. [CrossRef]
41. Pastero, L.; Massaro, F.R.; Aquilano, D. Experimental and theoretical morphology of single and twinned crystals of Li_2CO_3 (zabuyelite). *Cryst. Growth Des.* **2007**, *7*, 2749–2755. [CrossRef]
42. Aquilano, D.; Pastero, L. Anomalous mixed crystals: A peculiar case of adsorption/absorption. *Cryst. Res. Technol.* **2013**, *48*, 819–839. [CrossRef]
43. Pastero, L.; Giustetto, R.; Aquilano, D. Calcite passivation by gypsum: The role of the cooperative effect. *CrystEngComm* **2017**, *19*, 3649–3659. [CrossRef]
44. Pastero, L.; Aquilano, D.; Moret, M. Selective Adsorption/Absorption of Formamide in NaCl Crystals Growing from Solution. *Cryst. Growth Des.* **2012**, *12*, 2306–2314. [CrossRef]